

# Insights into the Heat-Assisted Intensive Light-Soaking Effect on Silicon Heterojunction Solar Cells

Weiyan Duan,\* Tobias Rudolph, Habtamu Tsegaye Gebrewold, Karsten Bittkau, Andreas Lambertz, Depeng Qiu, Muhammad Ainul Yaqin, Xixiang Xu, Kaining Ding,\* and Uwe Rau\*

Heat-assisted intensive light soaking has been proposed as an effective post-treatment to further enhance the performance of silicon heterojunction (SHJ) solar cells. In the current study, it is aimed to distinguish the effects of heat and illumination on different (doped and undoped) layers of the SHJ contact stack. It is discovered that both elevated temperature and illumination are necessary to significantly reduce interface recombination when working effectively together. The synergistic effect on passivation displays a thermal activation energy of approximately 0.5 eV. This is likely due to the photogenerated electron/hole pairs in the c-Si wafer, where nearly all of the incident light is absorbed. By distinguishing between the effects of light and heat effects on the conductivity of p- and n-type doped hydrogenated amorphous silicon (a-Si:H) layers, it is demonstrated that only heat is accountable for the observed rise in conductivity. According to numerical device simulations, the significant contribution to the open-circuit voltage enhancement arises from the reduced density of defect states at the c-Si/intrinsic a-Si:H interface. In addition, the evolution of the fill factor is highly dependent on changes in interface defect density and the band tail state density of p-type a-Si:H.

## 1. Introduction

Silicon heterojunction (SHJ) solar cells currently exhibit the highest efficiency among silicon-based devices. The cell efficiency has steadily improved in recent years and reached 26.8% for the two sides contacted structure as reported by Longi.<sup>[1]</sup> Due to its low-temperature processes, low-temperature coefficient, and high bifaciality, SHJ solar cell technology is considered promising for large-scale terrestrial PV applications.<sup>[2–4]</sup> The increasing commercial interest in SHJ solar cells has inspired research in further increasing the power conversion efficiency and understanding the underlying causal mechanisms.

Intrinsic and doped hydrogenated amorphous silicon (a-Si:H) layers are used for surface passivation and carrier selectivity, which are the key materials in SHJ solar cells for achieving high open-circuit voltage ( $V_{OC}$ ) and good carrier selectivity.<sup>[5]</sup>

Discovered by Staebler and Wronski in

1977, exposure to light can increase the defect density in a-Si:H, resulting in performance degradation in thin-film solar cells.<sup>[6,7]</sup> This effect raises concerns whether SHJ solar cells fabricated with ultrathin a-Si:H layers are stable under prolonged light exposure. Fortunately, in 2016, Kobayashi et al. reported an enhanced light-induced performance of SHJ solar cells under 1 sun illumination, which was attributed to a reduced density of recombination-active interface states, leading to an improvement in  $V_{OC}$  and fill factor (FF).<sup>[8]</sup> These authors also showed similar kinetics by applying a dark forward-voltage bias, where an increase in minority carrier injection in the absorber would be generated, which could contribute to near-interface state healing.<sup>[9,10]</sup> Multiple subsequent publications utilizing different light-soaking (LS) techniques have also revealed improvements in the efficiency of SHJ solar cells. These enhancements stem from systematic improvements in the  $V_{OC}$  and FF, as well as significant reductions in series resistance ( $R_s$ ).<sup>[11,12]</sup> Light-induced performance enhancement has been observed at the module level by several research groups, in addition to cell-level effects.<sup>[13,14]</sup> While some publications highlight the benefits of LS, there are also reports indicating harmful illumination effects. Wright et al. demonstrated a notable decline in the efficiency of commercial n-type SHJ solar cells when subjected to annealing

W. Duan, T. Rudolph, H. T. Gebrewold, K. Bittkau, A. Lambertz, D. Qiu, M. A. Yaqin, K. Ding, U. Rau  
IEK-5 Photovoltaik

Forschungszentrum Jülich GmbH  
52428 Jülich, Germany


E-mail: w.duan@fz-juelich.de; k.ding@fz-juelich.de; u.rau@fz-juelich.de

T. Rudolph, H. T. Gebrewold, D. Qiu, M. A. Yaqin, U. Rau  
Jülich Aachen Research Alliance (JARA-Energy) and Faculty of Electrical Engineering and Information Technology  
RWTH Aachen University  
52062 Aachen, Germany

X. Xu

LONGi Central R&D Institute

Longi Green Energy Technology Co., Ltd.  
Xi'an 710018, China

 The ORCID identification number(s) for the author(s) of this article can be found under <https://doi.org/10.1002/solr.202400383>.

© 2024 The Author(s). Solar RRL published by Wiley-VCH GmbH. This is an open access article under the terms of the Creative Commons Attribution-NonCommercial-NoDerivs License, which permits use and distribution in any medium, provided the original work is properly cited, the use is non-commercial and no modifications or adaptations are made.

DOI: 10.1002/solr.202400383

temperature above 85 °C under 1 sun illumination.<sup>[15]</sup> Cattin et al. found that the hole selectivity of the intrinsic/boron-doped layer stack is reduced when the *p*-type layer on the light-incoming side is not thick enough.<sup>[16]</sup> Therefore, efficiency changes vary significantly with different cell parameters under various combinations of elevated temperature and illumination. It is likely that various processes are stimulated by LS at elevated temperatures concurrently. Thus, a thorough comprehension of these processes is required to optimize SHJ devices for highest and stable performance.

In the studies cited, LS was predominantly applied under 1 sun conditions with prolonged treatment time and, at times, elevated temperature. Recently, several reports have proposed a high-intensity LS process that can be completed within minutes.<sup>[11,17]</sup> This process has emerged as a novel method for systematically enhancing the efficiency of SHJ solar cells within the industrial production process. In this study, our goal is to comprehensively understand the mechanism responsible for the heat-assisted intensive LS effect. We conduct experiments to differentiate the effects of thermal treatment and intense light illumination, which exhibit both independent and synergistic effects. We develop the SHJ solar cell layer stack methodically, examining the surface passivation and carrier transport characteristic in conduction heat-assisted intensive LS experiments. Finally, we employ finite-element method-based device simulations using Sentaurus Technology Computer Aided Design (TCAD) to analyze various defect densities within the device structure.

## 2. Results and Discussions

### 2.1. Process Decomposition

During the heat-assisted intensive LS process, the samples were heated on a hot table with a set temperature of 175 °C, under continuous illumination from light-emitting diodes (LED) for a duration of 90 s. The LED spectrum utilized has two prominent peaks centered at 450 and 600 nm, as shown in Figure S1A, Supporting Information. The spectral irradiance was adjusted to achieve a photon density that is equivalent to  $\approx 20$  suns. Incident light of this particular spectrum exhibits significant absorption and rapid intensity decay on the surface of the *n*-type silicon wafer, as shown in Figure S1B, Supporting Information. The absorption length has been determined using the absorption coefficient of a crystalline silicon (c-Si) wafer, listed in Figure S1C, Supporting Information. These findings suggest that there is almost no light penetrating through the SHJ solar cell fabricated on a 135  $\mu\text{m}$ -thick wafer. Unlike some 1 sun LS conditions, where the temperature was regulated below 50 °C, an elevated temperature was introduced in this experiment. This introduction needs careful consideration, particularly for the SHJ technology processed at low temperatures.<sup>[8,18]</sup> To have an idea about the temperature evolution during the LS process, the temperature profile on the samples was monitored using a pyrometer, and the results were plotted in Figure 1. The cells were transported through a track onto a preheated table under illumination. Thanks to the excellent thermal conductivity of silicon and the reliable temperature control system, the sample temperature experiences sharp increases (upon insertion) and decreases (upon removal) while maintaining a steady 210 °C throughout

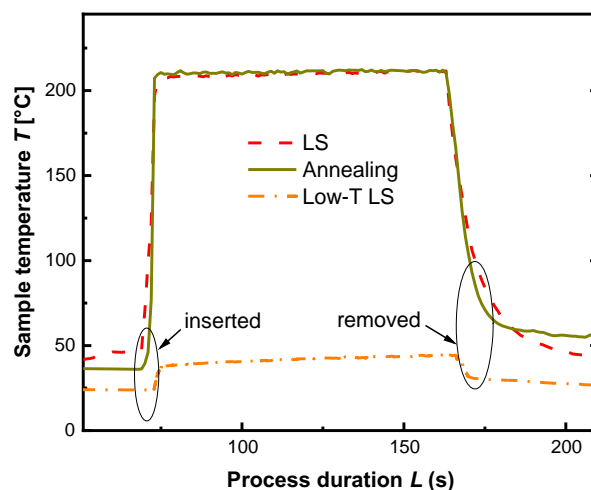


**Figure 1.** Sample temperature profiles during pure Annealing, Low-T LS, and LS processes.

the LS process. This high-intensity illumination rapidly increases the temperature of the sample, exceeding the table set temperature (175 °C) on the heated table.

Since a proper post-thermal treatment could also enhance the passivation and carrier transport in SHJ solar cells, what role does heat play in the LS process?<sup>[19,20]</sup> What occurs after absorption of high-intensity light in the first few micrometers of cells? To clarify these questions, three independent treatments were created for comparison: a pure heat process (Annealing), a low-temperature processed intensive LS (Low-T LS), and the heat-assisted intensive LS process. Figure 1 displays the sample temperature profiles under each treatment. The LED spectrum was switched off during the Annealing process. The table heating temperature was elevated to attain the same thermal budget on the samples as in the LS condition. It is evident that the two curves (red and brown) overlap well. In the Low-T LS process, the table heating was deactivated. Even though light exposure increases the temperature of the sample, the final sample temperature remains below 45 °C due to the short 90 s process time. As a result, the samples are minimally affected by thermal conditions.

### 2.2. SHJ Solar Cell Performance

First, we conducted LS on two types of bus-bar-less SHJ solar cells from the *n* side. The two cell types differ in the *p*-side interface treatment during fabrication. Specifically, “cell type 1” received a hydrogen plasma pretreatment to improve the c-Si surface cleaning before intrinsic a-Si:H (a-Si:H (i)) deposition, while “cell type 2” did not undergo such a process.<sup>[21]</sup> Figure 2 shows the pre- and post-process current–voltage (*I*–*V*) characteristics for each group using box plots, along with the absolute change in each parameter. The average efficiency improves by 0.15%<sub>abs</sub> and 0.50%<sub>abs</sub> for “cell type 1” and “cell type 2”, respectively. The increase in efficiency can be attributed to the improvement of both the *V*<sub>OC</sub> and FF in both cell types. However, the short-circuit current density (*J*<sub>SC</sub>) did not show any statistically significant changes. The improvement in “cell type 2” under the applied LS condition is considerably better than what was previously reported under

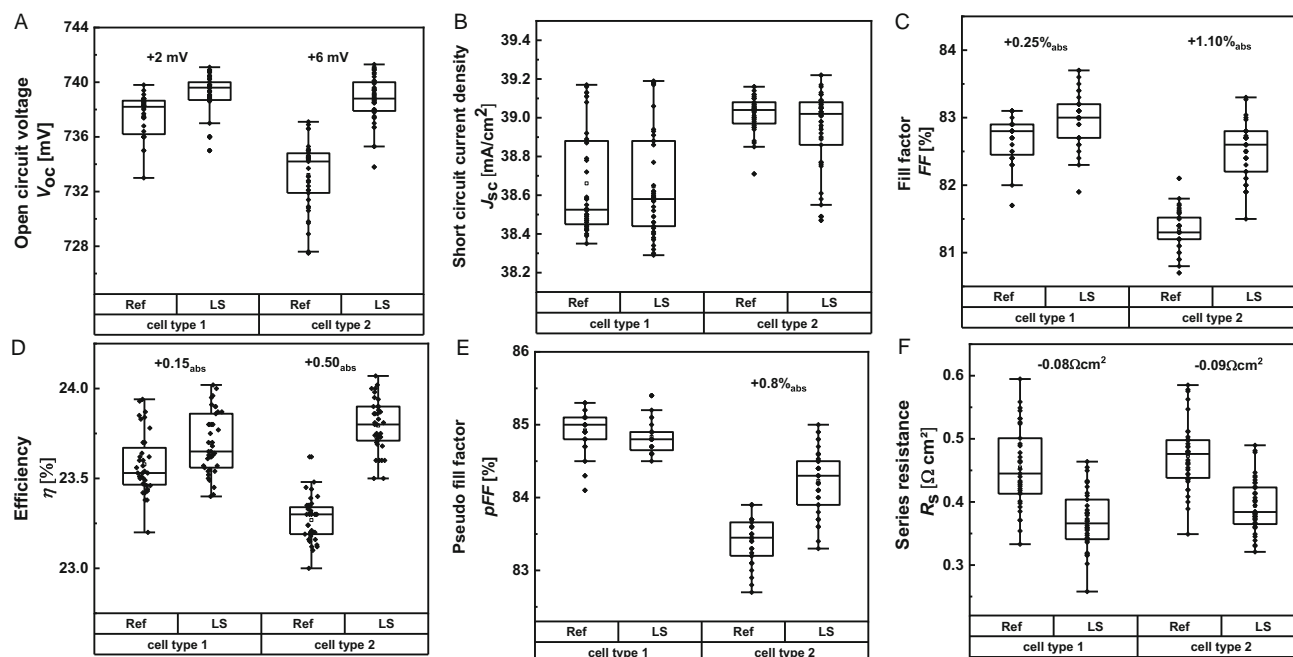


**Figure 2.** A)  $V_{OC}$ , B)  $J_{SC}$ , C) FF, D) efficiency, E)  $pFF$ , and F)  $R_S$  of two types SHJ solar cells before and after LS. The values are based on more than 20 M2+ industrial sized cells per batch. The light was incident from n side.

1 sun illumination. This demonstrates a promising pathway for improving efficiency, even with an initial average cell efficiency exceeding 23.3%.<sup>[8,9]</sup> A deeper analysis of the light-induced changes reveals distinctive origins for each of the two cell types. The different initial  $V_{OC}$ s for the two cell types indicate that the different cell fabrication techniques result in different effects on the passivation process. A more pronounced  $V_{OC}$  increase occurs for “cell type 2” compared to “cell type 1”. The improved passivation of “cell type 2” after LS significantly enhances its pseudo FF ( $pFF$ ), which measures FF without  $R_S$  loss. Here, the  $R_S$  values were determined through  $I$ - $V$  measurements at varying illumination intensities. The  $R_S$  was reduced by the same magnitude for both types of cells, contributing to the FF improvement. It is noteworthy that the stronger increase of FF in “cell type 2” arises not only from the lowered  $R_S$ , but also from the substantial enhancement in  $pFF$ , which is not the case for “cell type 1”. In the latter,  $R_S$  dominates the slight variation of FF. The corresponding  $R_S$ -driven FF gain calculated as  $\Delta FF_{R_S} = \Delta(pFF - FF)$  was determined to be roughly 0.3%<sub>abs</sub> for “cell type 2”. It can be seen that a decrease in  $R_S$  and an enhanced passivation led to  $\approx 28\%$  and  $\approx 72\%$  of the overall FF gain (1.1%<sub>abs</sub>), respectively. The impact of LS on solar cell performance is greatly influenced by processing conditions, specifically the initial state of SHJ solar cells. As we observed a decrease in resistance that was identical between both cell types, but a notably greater increase in  $V_{OC}$  in “cell type 2”, this study will mainly focus on examining the evolution of passivation and carrier transport for “cell type 2”.

### 2.3. Heat-Assisted Light-Induced $V_{OC}$ Enhancement

To investigate the origin of enhanced  $V_{OC}$  after LS, we analyzed various samples with symmetric passivation layers, such as a-Si:

H (i) structure (i/i), a-Si:H (i)/n-type a-Si:H (a-Si:H (n)) structure (i-n/i-n), and a-Si:H (i)/p-type a-Si:H (a-Si:H (p)) (i-p/i-p) structure. In **Figure 3**, we show how the excess carrier lifetime ( $\tau_{eff}$ ) of these symmetric structures develops after Annealing, Low-T LS, and LS processes at the carrier injection level of  $1 \times 10^{15} \text{ cm}^{-3}$ . The  $\tau_{eff}$  of the i/i and i-n/i-n samples both increase after Annealing treatment, as demonstrated in **Figure 3A,B**. This phenomenon can be explained by the effects of isothermal Annealing on the microstructural Si-H bonding environment, which promotes the passivation of the c-Si/a-Si:H interfaces.<sup>[22,23]</sup> In contrast, the  $\tau_{eff}$  of the i-p/i-p structure shows a slight decrease after Annealing as shown in **Figure 3C**. This phenomenon may be attributed to the Fermi energy-dependent defect generation in the a-Si:H (p) films during annealing.<sup>[24]</sup> The surface passivation of the i/i structures appears to degrade slightly after Low-T LS, consistent with Kobayashi’s research, and can be explained by the Staebler-Wronski effect (SWE), where light creates defects in the a-Si:H bulk that trigger electron-hole recombinations.<sup>[25,26]</sup> For samples passivated by doped layers (i-n/i-n and i-p/i-p),  $\tau_{eff}$  values either slightly improved or remained stable after Low-T LS. The presence of the doped layer shifts the Fermi level toward one of the band edges, which may reduce or even reverse the negative SWE upon passivation.<sup>[24]</sup> We conclude that this enhancement, induced by light at low temperatures, must compete with the potentially negative SWE upon passivation. Remarkably, the  $\tau_{eff}$  of all structures increases twofold following the LS treatment. After observing the  $\tau_{eff}$  evolution of the symmetrical structures under the three different treatments, it is clear that the LS effect is not a simple superposition of Annealing and Low-T LS. Rather, it is a synergistic effect. The significant improvement of  $\tau_{eff}$  in i/i samples suggests that the passivation enhancement by LS can be attributed to the change in interface states density between c-Si

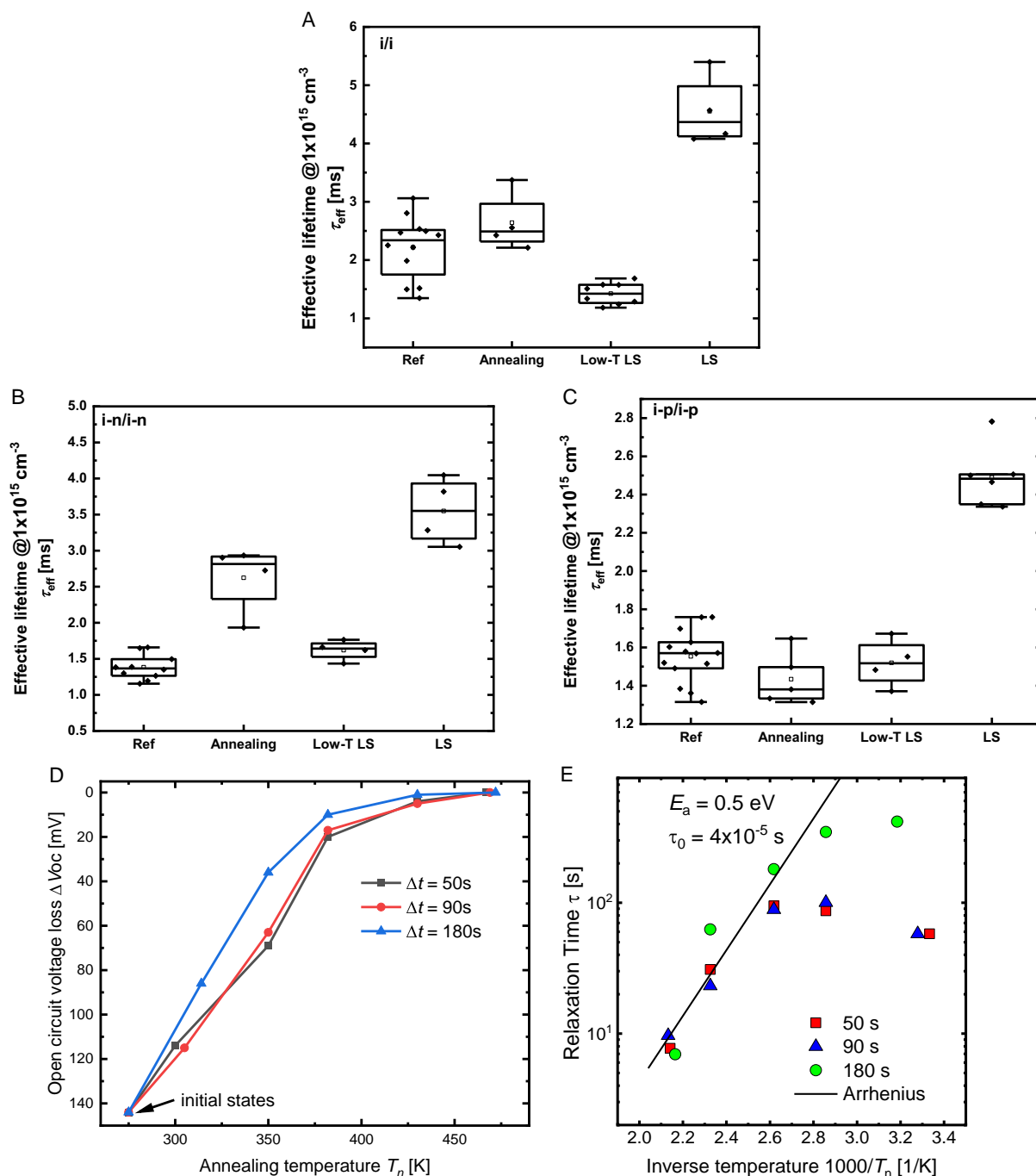


**Figure 3.** Changes in the minority carrier lifetime for samples with A) i/i, B) i-n/i-n, and C) i-p/i-p symmetric structure. The evaluation was performed at the carrier injection of  $1 \times 10^{15} \text{ cm}^{-3}$ . D) Isochronal LS experiments with time steps 50, 90, and 180 s for ITO sputtered i-n/i-n samples. E) Arrhenius plot of the restored time constants  $\tau_n$  gained from the isochronal LS experiments with different time steps.

and a-Si:H (i) interface as well as the defects density in the a-Si:H (i) bulk.

Isochronal LS cycles with different time steps were performed to calculate the activation energy and examine how the LS process heals passivation. The isochronal LS process began with i-n/i-n samples, which were coated on both sides with Sn-doped indium oxide (ITO). The sputtering process caused a significant

implied  $V_{oc}$  (i $V_{oc}$ ) loss. The samples underwent LS for a fixed time increment of  $\Delta t$ , with temperatures increasing successively by  $\Delta T$  of  $\approx 40 \text{ K}$ . The initial temperature was room temperature, and the final temperature was where the i $V_{oc}$  reached saturation. During the intervals between LS, measurements were taken on the lifetime and i $V_{oc}$  of the samples. Figure 3D depicts the relationship between the  $V_{oc}$  loss ( $\Delta V_{oc}$ ) and the LS process at

different substrate temperatures, with  $\Delta t$  values of 50, 90, and 180 s. Even though room temperature was maintained for all samples during the lowest LS temperature, the light-induced thermal effect caused a slight increase in the actual temperature of the sample. When the LS temperature is lower than 400 K, increasing the Annealing temperature leads to a considerable reduction in  $\Delta V_{OC}$ , indicating a rapid restoration of passivation quality. For instance, even for low temperatures such as 314 K,  $\Delta V_{OC}$  reduces from 146 to 86 mV for the sample light soaked for  $\Delta t = 180$  s. This strongly suggests that light has a significant impact on the entire process.

To calculate the relaxation time  $\tau$ , we computed the excess defect concentration  $N_{exc}(n)$  after each LS process using the  $\Delta V_{OC}$  values presented in Figure 3D. The relaxation time constant  $\tau_n(T_n)$  at the LS temperature  $T_n$  can be determined by analyzing the changes in  $N_{exc}$  caused by LS and can be expressed as  $\tau_n = \Delta t / \ln\{N_{exc}(n-1)/N_{exc}(n)\}$ .<sup>[27]</sup> The use of three different time steps allows a greater range of relaxation times to be covered. Figure 3E depicts an Arrhenius plot of the relaxation time  $\tau_n$  against the  $1000/T_n$  during the corresponding LS interval. It is found that the relaxation time can be described according to  $\tau_n = \tau_0 \exp(E_A/kT_n)$  with  $E_A = 0.5$  eV and  $\tau_0 = 4 \times 10^{-5}$  s. The activation energy is about 12 times the thermal energy at 210 °C.<sup>[28]</sup> This shows that the intensive light during the process requires the support of heat to restore passivation. An identical  $V_{OC}$  gain was observed after LS, regardless of whether the illumination originated from the hole or electron contact side, as illustrated in Figure S2, Supporting Information. As the intense light gets mostly absorbed in the illuminated contacting stack and the first several micrometers of c-Si, the findings suggest that the passivation enhancement is not due to the absorption of photons in the front-contacting stacks. Instead, it could be because of the absorption of photons in the bulk of the wafer since it is independent of the illumination side. Similar to Kobayashi et al.'s study demonstrating that carrier injection during 1 sun LS enhances passivation,<sup>[8]</sup> the increased carrier injection from the wafer bulk during heat-assisted intensive LS should also contribute to passivation enhancement. The high carrier concentration can partially recombine through charged trap states in the a-Si:H thin films, releasing energy to reconstruct the interface microstructure. Eventually, thermally activated hydrogen movement allows for the passivation of interface defects after the recombination process. This reduces the density of defects and enhances the performance of solar cells.

#### 2.4. Heat-Assisted Light-Induced $R_s$ Reduction

Next, we examine the source of the  $R_s$  reduction in our cell device to understand how carrier transport is enhanced by the heat-assisted intensive LS process. When one side of the solar cell is illuminated by intense light, only thermal effects can influence the opposite side of the solar cell. This is due to the fact that the light cannot penetrate through the bulk of the wafer as previously discussed. Surprisingly, a very similar absolute  $R_s$  reduction was observed after the LS process, as shown in Figure 4A, regardless of whether the n side or p side was illuminated. In an SHJ solar cell,  $R_s$  is the average lumped resistance that a charge carrier

experiences through its path inside the solar cell. This includes the transport loss through the wafer bulk, the interfaces between thin-film layers, the lateral collection to the grid, the contact with the metallization grid and the grid itself.<sup>[29]</sup> The capacitance–voltage measurement results shown in Figure S3, Supporting Information, demonstrate that the resistivity of the wafer bulk remains unchanged after the LS process, as indicated by two nearly coinciding curves. The transport losses in the grid can also be disregarded due to the application of a finger resistivity neglecting contacting scheme to measure the bus-bar-less solar cell, which is similar to the one utilized at the Institut für Solarenergieforschung in Hameln's (ISFH's) CalTec.<sup>[30]</sup> To gain insight into the localization of light-induced reduction of  $R_s$ , we conducted the transfer-length-method (TLM) measurement. This method extracted total vertical contact resistivity from both sides of the solar cells. Figure S4, Supporting Information, displays the TLM measurement structures, utilizing n-type wafers and p-type wafers to determine contact resistivity on the n side and p side, respectively. Thanks to the optimized metallization process, the contact resistivity between ITO and Ag is too low to be measured properly by the TLM method. Thus, the primary contribution to the contact resistivities shown in Figure S4, Supporting Information, derives from the contact resistivities between ITO and a-Si:H (n) and ITO and a-Si:H (p), respectively. The TLM measurement results are presented in Figure 4B,C, with “face table” and “face light” denoting whether the TLM pattern is oriented toward the heating table or the light source during the LS process. In addition, “face table” implies similar conditions as for pure Annealing. The specific contact resistivity between ITO and a-Si:H(n) reduces from an average value of 125 to 100 m $\Omega$  cm<sup>2</sup> for both cases, which shows a similar trend to that of p-type samples where the average value of 150 m $\Omega$  cm<sup>2</sup> drops to 110 m $\Omega$  cm<sup>2</sup>. This explains and correlates well with the information displayed in Figure 4A. As depicted in Figure 2F, the average total drop in  $R_s$  is  $\approx 90$  m $\Omega$  cm<sup>2</sup> after undergoing the LS process. This indicates that about 44% of the improvement arises from improved vertical transport at the p-side due to the thermal effect, and  $\approx 28\%$  results from the illuminated n-side. The remaining portion can be attributed to enhanced lateral carrier collection by the more conductive ITO, as will be shown later.

The dark conductivity of doped a-Si:H layers and the sheet resistance ( $R_{sh}$ ) of ITO were further investigated to uncover the underlying mechanism behind the reduced contact resistivities. Since the samples for conductivity measurement were prepared on Corning Eagle 2000 glass substrates, which have lower thermal conductivity than silicon wafers, the film sides were adhered to a silicon wafer using Ag paste to ensure proper thermal conductance with the table during the short process. Please refer to Figure S5, Supporting Information, for a detailed schematic. The glass substrate allows for over 90% transmittance at 450 and 600 nm emission peaks, enabling most of the light to pass through to reach the film layers. Figure 5 displays the electrical properties of doped a-Si:H layers and ITO undergoing different treatments. The average dark conductivity of the a-Si:H (n) layer increases from  $1.4 \times 10^{-3}$  to  $5.0 \times 10^{-3}$  S cm<sup>-1</sup> with all the treatments applied to the samples. A similar trend is also found in a-Si:H (p) thin films, with an increase in the average dark conductivity from  $7.1 \times 10^{-6}$  to  $2.0 \times 10^{-5}$  S cm<sup>-1</sup>. The  $R_{sh}$



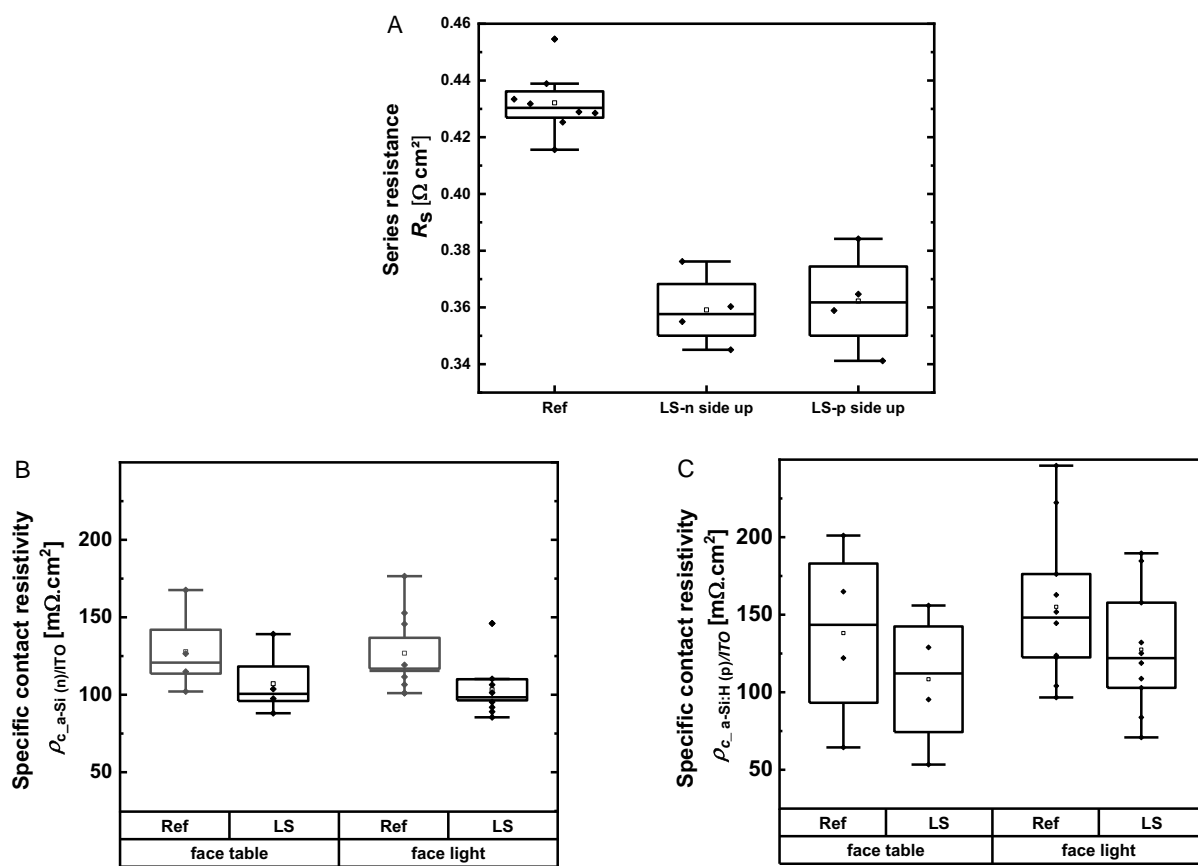


**Figure 4.** A)  $R_S$  evolution when cells are illuminated from n side or p side under heat-assisted intensive light-soaking process. TLM measurement results showing the variations in B) electron contact resistivity and C) hole contact resistivity when the structures are facing the table or facing the light during the heat-assisted intensive light-soaking process.

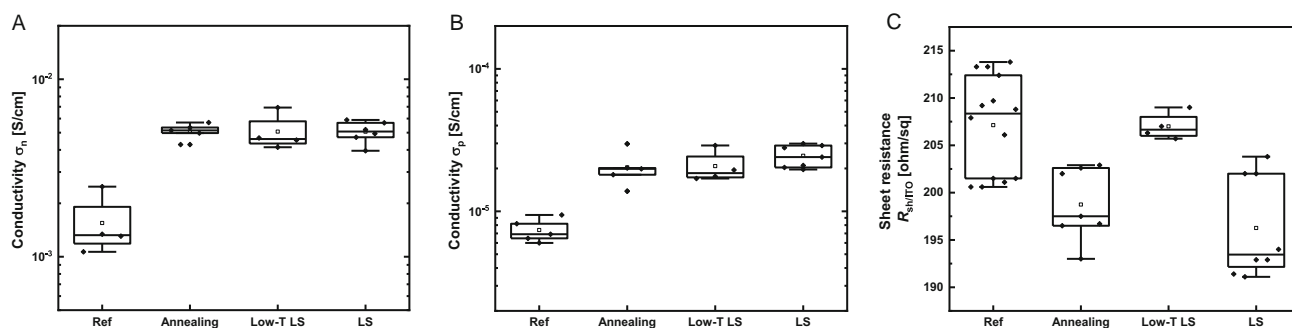


**Figure 5.** Conductivity changes of A) a-Si:H (n), B) a-Si:H (p), and C) sheet resistance changes of ITO thin films after treated with "Annealing," "Low-T LS," and "LS" processes separately.

of ITO decreases from  $\approx 208$  to  $\approx 195 \Omega \text{ sq}^{-1}$  after Annealing or LS processes. This differs from Low-T LS, where the values remain constant. This demonstrates that the improvement in ITO conductivity results solely from the heat effect. The consistent evolution trend after Annealing and LS processes for these three thin films can well explain the TLM results mentioned earlier. The increase in dark conductivity observed in a-Si:H (n) and a-Si:H (p) due to Low-T LS can be explained as a light-induced improvement in doping efficiency.<sup>[31–33]</sup> Taking a-Si:H (p) as an

example, atomic hydrogen can deactivate boron acceptors by forming weak H–B–Si components. The intensive LS can promote the diffusion and hopping of these weakly bound hydrogen atoms, so that the increase in the B–H mode will be obtained and efficient B–Si<sub>4</sub> doping can be activated.<sup>[31,32]</sup> While light-induced creation of dangling bonds typically results in decreasing dark conductivity in a-Si:H (i) and lightly doped a-Si:H layers, the high dopant concentrations utilized in this study for the doped layers can quench this effect.<sup>[6,34]</sup> It should be noted that the

observed increase in conductivity for the Annealing and Low-T LS cases is merely a coincidence. The magnitude of the conductivity increase is related to the nature of the thin film itself and process conditions. However, the light-induced changes in conductivity can be completely annealed out with adequate heat treatment.<sup>[33]</sup> This may explain why the LS treatment does not offer additional conductivity enhancement compared to the Annealing process. To confirm the dominance of thermal effects in reducing  $R_s$  during the LS, one group of solar cells cured at 170 °C for 40 min underwent the extra Annealing process and were then subjected to LS again. As shown in Figure S6, Supporting Information, the  $R_s$  values drop significantly after Annealing. However, with the additional LS step, no further reduction in  $R_s$  values was observed. From the above findings, it can be inferred that the decrease in  $R_s$  values after the LS process only occurs when the SHJ solar cells have not been sufficiently treated. Thus, even though illumination could increase the conductivity of heavily doped layers, it is still mainly driven by the thermal effect here.

## 2.5. Insights from Simulation

Summarizing the aforementioned information, we conclude that the changes induced in SHJ solar cells by heat-assisted intensive LS occur in the thin-film layers and at the interfaces situated on the n-type c-Si wafer. The gain in efficiency after LS is primarily due to an increased  $V_{oc}$  and FF as a result of improved passivation and carrier transport. To further quantify and confirm the impact of individual layer and interface properties, we use Sentaurus TCAD device simulation tool to vary the defect densities at different positions in the device structure, to determine the possible individual contribution from each layer or interface and

explain the observed effects from the LS process.<sup>[35]</sup> The detailed input parameters for the simulation can be found in Table S1 and S2, Supporting Information. **Figure 6** illustrates the performance of SHJ solar cells while varying the density of the band tail states in doped and intrinsic a-Si:H layers as well as the interface defect density between c-Si and a-Si:H (i). The changes in conductivity in doped a-Si:H are assumed to result from the impact of the density of band tail states on the concentration of charge carriers. The solid lines with solid symbols denote an interface defect density of  $D_{it} = 1 \times 10^{10} \text{ cm}^{-2} \text{ eV}^{-1}$ , which corresponds to “cell type 2” before LS. The dashed lines with cross symbols denote an interface defect density of  $D_{it} = 3 \times 10^9 \text{ cm}^{-2} \text{ eV}^{-1}$ . The shaded area depicts the interesting region for SHJ solar cells in this work, as all the cell parameters presented in Figure 2 come under this range. As can be seen from Figure 6A, to increase the  $V_{oc}$  by 6 mV for “cell type 2”, it can be obtained by reducing the band tail states density in a-Si:H (p) (red solid line) or reducing the interface defect density (from the solid lines to the dash lines). However, the variation in the band tail states density in a-Si:H (p) will cause a much more substantial FF change as depicted in Figure 6B, contradicting the measured results after LS. Only by changing the interface defect density to  $D_{it} = 3 \times 10^9 \text{ cm}^{-2} \text{ eV}^{-1}$ , a good agreement with the measured solar cell parameters for “cell type 2” after LS be achieved. Therefore, the gain in  $V_{oc}$  has to be explained by a decrease in the interface defect density between c-Si and a-Si:H (i), which results in enhanced surface passivation. This finding is supported by the significant improvement in  $\tau_{eff}$  after LS in the contactless (without doped layers) i/i structure, as previously shown in Figure 3A.

Deeper insights are shown in the contour plots of  $V_{oc}$  and FF as a function of band tail state density in a-Si:H (p) and interface defect density in Figure S7, Supporting Information. Assuming

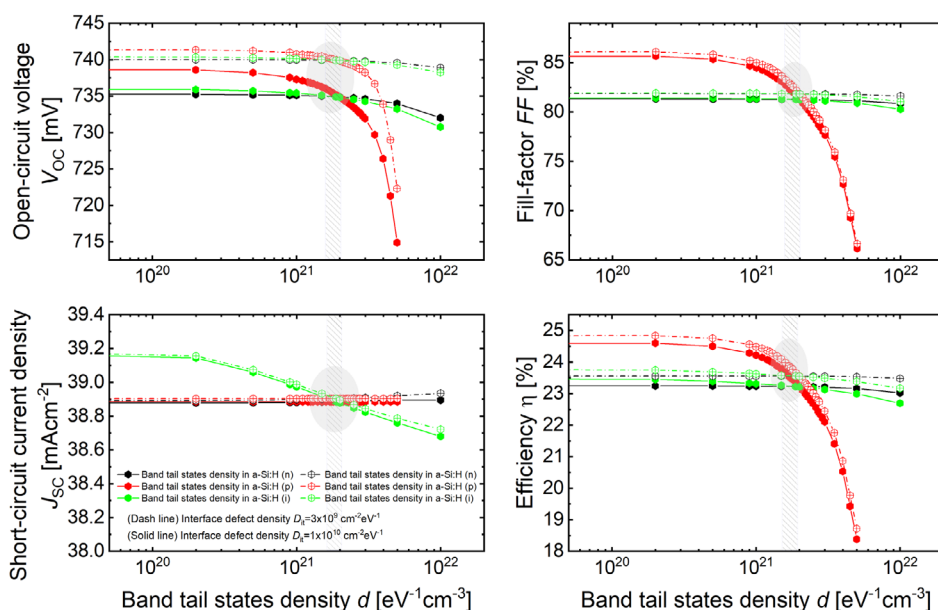


**Figure 6.** Effects of band tail states density (Urbach tail pre-factor in  $\text{cm}^{-3} \text{ eV}^{-1}$ , see Table S2, Supporting Information) in doped and intrinsic a-Si:H layers and interface defect density  $D_{it}$  ( $\text{cm}^{-2} \text{ eV}^{-1}$ ) on SHJ solar cells performance. Dash lines with cross symbol represent effect from interface defect density of  $D_{it} = 3 \times 10^9 \text{ cm}^{-2} \text{ eV}^{-1}$ , and solid lines with solid symbol represent effect from interface defect density of  $D_{it} = 1 \times 10^{10} \text{ cm}^{-2} \text{ eV}^{-1}$ . The shaded area depicts the interesting region for SHJ solar cells in this work.

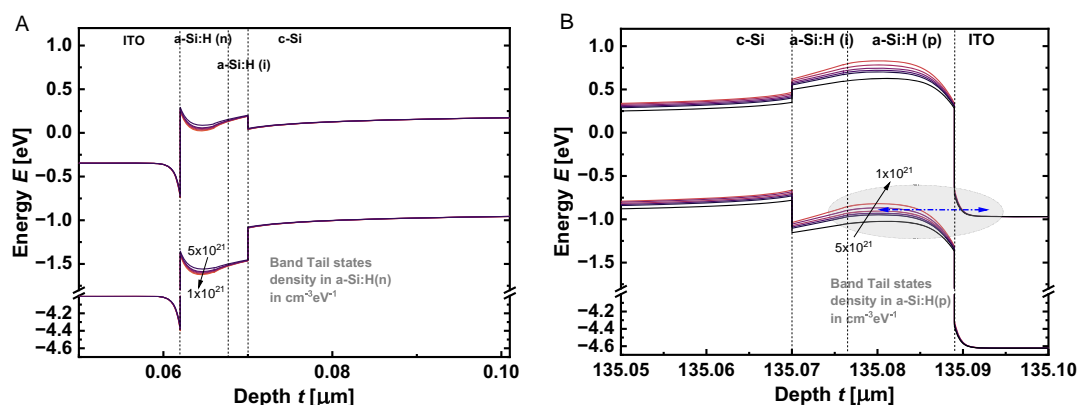


**Figure 7.** Band diagrams of SHJ solar cells working at MPP point when varying the band tail states densities in A) a-Si:H (n) and B) a-Si:H (p) layers.

conductivity of a-Si:H (p) and interface defect density are the predominant factors, band tail state density is estimated before and after LS, with values extracted from Figure S7, Supporting Information, to be from  $2.03 \times 10^{21}$  to  $1.75 \times 10^{21} \text{ cm}^{-3} \text{ eV}^{-1}$ . From the difference between the quasi-Fermi level energy and the valence band energy, we extracted the relative change in conductivity for those two band tail state densities, resulting in a factor of  $\approx 2.4$  (after vs before LS, cf. Figure S8, Supporting Information). This is in very good agreement with the  $\approx 2.8$  factor improvement of the measured average conductivity of a-Si:H (p) as shown in Figure 5, which proves the reliability of the simulation, supporting the drawn conclusions.

For the FF evolution, Figure 6B shows a strong dependency on the band tail states density in a-Si:H (p). To understand this impact on FF, band diagrams of SHJ solar cells at 620 mV bias, near the maximum power point (MPP), for different band tail states densities in the doped a-Si:H layers are simulated and plotted in Figure 7. As shown in Figure 7B, the reduction of the band tail states density in a-Si:H (p) shows a significant band shift due to enhanced free charge carriers. As a result, better alignment of the valence band of a-Si:H (p) and the conduction band of ITO can be obtained. Thus, there will be a higher contribution of band-to-band tunneling and less dependency on trap-assisted tunneling, which results in improved carrier transport between a-Si:H (p) and ITO. This is also verified by the measured  $40 \text{ m}\Omega \text{ cm}^2$  reduction in contact resistance, as presented in Figure 4C. From Figure 7A, the decrease of the band tail states density in a-Si:H (n) could also result in a slightly better band alignment between the conduction bands of a-Si:H (n) and ITO, which explains the reduced  $25 \text{ m}\Omega \text{ cm}^2$  contact resistance, as shown in Figure 4B. Obviously, the reduction of band tail states density (or the increase of conductivity) in a-Si:H (p) has a greater impact on the enhancement of carrier transport (or  $R_s$  reduction) after LS compared to a-Si:H (n). To find out whether the change of band tail states density in doped layers affects field-effect passivation, the minority carrier densities on both surfaces of c-Si were plotted as shown in Figure S9, Supporting Information. For the n side, the hole density reduces from  $3 \times 10^{12}$  to  $2 \times 10^{12} \text{ cm}^{-3}$  on the surface of c-Si; for the p side, there is a more obvious drop in electron density from  $5 \times 10^{13}$  to  $6 \times 10^{11} \text{ cm}^{-3}$  when the band tail states density

reduces from  $5 \times 10^{21}$  to  $1 \times 10^{21} \text{ eV}^{-1} \text{ cm}^{-3}$ . More effective blocking of minority carrier transport implies better field-effect passivation. Thus, changes in the density of band tail states in a-Si:H (p) can have a higher impact on field-effect passivation compared to a-Si:H (n). However, this improved field-effect passivation in a-Si:H (p) has a limited effect on  $V_{OC}$  gain, as demonstrated in Figure S7A, Supporting Information. But it contributes to the FF gain, similar to reduced interface defect density as shown in Figure S7B, Supporting Information; by looking at the region we are interested in. As discussed previously,  $\approx 72\%$  of the overall FF gain in “cell type 2” arises from the passivation improvement. This passivation improvement mainly resulted from the reduced interface defect density which contributes to the chemical passivation and increased conductivity in a-Si:H (p) which contributes to the field-effect passivation.

### 3. Conclusions

The present detailed investigation of heat-assisted LS of SHJ solar cells establishes that at least two distinct mechanisms are at work under the usually applied conditions for LS (enhanced temperature and larger than 1 sun light intensity). Summary key impact factors for solar cell performance improvement can be found in Figure S10, Supporting Information. One mechanism is directly connected to the passivation quality of the interface between the c-Si wafer and the a-Si:H: i) passivation layer as demonstrated by the lifetime enhancement in samples that even have no doped layers. This effect clearly requires both enhanced temperature and illumination. We argue that the effect is due to the passivation of Si-dangling bonds at or close to the amorphous/crystalline interface by hydrogen atoms or molecules abundantly available close to the interface region of the device. This passivation effect is mediated by the recombination of photogenerated electron-hole pairs taking place precisely at these dangling bonds and, therefore, would be a self-limiting process for interface recombination. The second mechanism is the enhancement of the active doping density in the n- and p-type doped layers. This process is driven by the enhanced temperature without the need for illumination. Note that even though a light-induced conductivity increase was found for doped a-Si:H layers, this effect may be annealed out by the heating effect. Our



numerical simulations show that the  $V_{OC}$  improvement stems from the reduced defect state density at the c-Si/a-Si:H: i) interface rather than the conductivity increase in doped layers. The reduction of interface defect density and the enhanced electrostatic effect in the doped layers are both responsible for the FF enhancement. Among them, the passivation of interface defect density and doping in a-Si:H (p) play more prominent roles.

## Supporting Information

Supporting Information is available from the Wiley Online Library or from the author.

## Acknowledgements

The authors would like to thank the support from Alain Doumit for the wafer texture and cleaning, Volker Lauterbach for the a-Si:H depositions, Siekmann for the ITO sputtering, and Silke Lynen for the screen printing. They specially thank Dr. Wolfhard Beyer for the nice discussion on the role of hydrogen in amorphous silicon. Dr. Beyer is an outstanding scientist, a patient teacher, and a kindhearted person. The authors will always remember him in this way. The work will also follow his good example in the future. This work was supported by the German Federal Ministry of Economic Affairs and Energy in the framework of the TOUCH project (grant no. 0324351) and the (HEMF) Helmholtz Energy Materials Foundry infrastructure funded by the HGF (Helmholtz association). The authors are grateful for the high-quality wafers supply by the LONGI company.

## Conflict of Interest

The authors declare no conflict of interest.

## Author Contributions

W. D. and K. D. conceived the project. W. D., T. R., and U. R. designed the experiments. T. R. conducted the device and thin-film characterization. H. T. G., K. B., and W. D. carried out the device simulations. A. L., D. Q., and M. A. Y. organized and fabricated the SHJ solar cells and thin-film samples. W. D. and U. R. supervised the research. W. D. wrote the manuscript and K. B. improved the language. All authors were involved in the discussion of the results.

## Data Availability Statement

The data that support the findings of this study are available on request from the corresponding author. The data are not publicly available due to privacy or ethical restrictions.

## Keywords

defects, heats, light soakings, silicon heterojunctions, thin films

Received: May 22, 2024

Revised: August 5, 2024

Published online: September 2, 2024

- [1] M. A. Green, E. D. Dunlop, G. Siefer, M. Yoshita, N. Kopidakis, K. Bothe, X. Hao, *Prog. Photovolt.* Early View.
- [2] A. Razaq, T. G. Allen, W. Liu, Z. Liu, S. De Wolf, *Joule* **2022**, 6, 514.
- [3] Y. Liu, Y. Li, Y. Wu, G. Yang, L. Mazzarella, P. Procel-Moya, A. C. Tamboli, K. Weber, M. Boccard, O. Isabella, X. Yang, B. Sun, *Mater. Sci. Eng. R Rep.* **2020**, 142, 100579.
- [4] J. Haschke, O. Dupre, M. Boccard, C. Ballif, *Sol. Energy Mater. Sol. Cells* **2018**, 187, 140.
- [5] S. De Wolf, A. Descoedres, Z. C. Holman, C. Ballif, *Green* **2012**, 2, 7.
- [6] D. L. Staebler, C. R. Wronski, *Appl. Phys. Lett.* **1977**, 31, 292.
- [7] H. Plagwitz, B. Terheiden, R. Brendel, *J. Appl. Phys.* **2008**, 103, 094506.
- [8] E. Kobayashi, S. D. Wolf, J. Leprat, G. Christmann, A. Descoedres, S. Nicolay, M. Despeisse, Y. Watabe, C. Ballif, *Appl. Phys. Lett.* **2016**, 108, 153503.
- [9] E. Kobayashi, S. D. Wolf, J. Leprat, A. Descoedres, M. Despeisse, F. Haug, C. Ballif, *Sol. Energy Mater. Sol. Cells* **2017**, 173, 43.
- [10] S. Olibet, E. Vallat-Sauvia, C. Ballif, *Phys. Rev. B* **2007**, 76, 035326.
- [11] S. Bao, L. Yang, J. Huang, Y. Bai, J. Yang, J. Wang, L. Lu, L. Feng, X. Bai, F. Ren, D. Li, H. Jia, *J. Mater. Sci. Mater. Electron.* **2021**, 32, 4045.
- [12] J. Veirman, A. J. K. Leoga, L. Basset, W. Favre, O. Bonino, A. L. Priol, N. Rochat, D. Rouchon, *AIP Conf. Proc.* **2022**, 2487, 020017.
- [13] E. Fokuhl, T. Naeem, A. Schmid, P. Gebhardt, T. Geipel, D. Philipp, in *36th EU PVSEC*, September **2019**, Marseille, France.
- [14] J. Yu, P. S. Leonard, D. Qiu, Y. Zhao, A. Lambert, C. Zahren, V. Lauterbach, W. Duan, J. Yu, K. Ding, *Sol. Energy Mater. Sol. Cells* **2022**, 235, 111459.
- [15] B. Wright, C. Madumelu, A. Soeriyadi, M. Wright, B. Hallam, *Sol. RRL* **2020**, 2000214.
- [16] J. Cattin, L. Senaud, J. Haschke, B. Paviet-Salomon, M. Despeisse, C. Ballif, M. Boccard, *IEEE J. Photovolt.* **2021**, 11, 575.
- [17] M. Wright, A. Soeriyadi, B. Wright, D. Andronikov, I. Nyapshaev, S. Abolmasov, A. Abramov, B. Hallam, *IEEE J. Photovolt.* **2022**, 12, 267.
- [18] J. Cattin, D. Petri, J. Geissbühler, M. Despeisse, C. Ballif, M. Boccard, *IEEE J. Photovolt.* **2021**, 11, 575.
- [19] J. W. A. Schütttauf, C. H. M. van der Werf, I. M. Kielen, W. G. J. H. M. van Sark, J. K. Rath, R. E. I. Schropp, *J. Non Cryst. Solids* **2012**, 358, 2245.
- [20] C. Luderer, C. Messmer, M. Hermle, M. Bivour, *IEEE J. Photovolt.* **2020**, 10, 952.
- [21] S. N. Granata, T. Bearda, F. Dross, I. Gordon, J. Poortmans, R. Mertens, *Solid State Phenom.* **2012**, 195, 321.
- [22] S. De Wolf, S. Olibet, C. Ballif, *Appl. Phys. Lett.* **2008**, 93, 032101.
- [23] T. F. Schulze, H. N. Beushausen, C. Leendertz, A. Dobrich, B. Rech, *Appl. Phys. Lett.* **2010**, 96, 252102.
- [24] S. De Wolf, M. Kondo, *J. Appl. Phys.* **2009**, 105, 103707.
- [25] M. Stutzmann, *Philos. Mag. B* **1989**, 60, 399.
- [26] E. M. El Mhamdi, J. Holovsky, B. Demareux, C. Ballif, S. De Wolf, *Appl. Phys. Lett.* **2014**, 104, 252108.
- [27] A. Jasenek, H. W. Schock, J. H. Werner, U. Rau, *Appl. Phys. Lett.* **2001**, 79, 1415345.
- [28] <https://en.m.wikipedia.org/wiki/Electronvolt> (assecced: December 2023).
- [29] L. Basset, W. Favre, D. Munoz, J. P. Vilcot, *35th EU PVSEC*, September **2018**, Brussels.
- [30] K. Bothe, C. Kruse, D. Hinken, R. Brendel, *37th EU PVSEC*, September **2020**, Lisbon.
- [31] J. Jang, S. C. Park, S. C. Kim, *Appl. Phys. Lett.* **1987**, 51, 1804.

- [32] W. Liu, J. Shi, L. Zhang, A. Han, S. Huang, X. Li, J. Peng, Y. Yang, Y. Gao, J. Yu, K. Jiang, X. Yang, Z. Li, W. Zhao, J. Du, X. Song, J. Yin, J. Wang, Y. Yu, Q. Shi, Z. Ma, H. Zhang, J. Ling, L. Xu, J. Kang, F. Xu, J. Liu, H. Liu, Y. Xie, F. Meng, et al., *Nat. Energy* **2022**, 7, 427.
- [33] X. Li, Y. Xiong, Y. Yang, S. Huang, K. Jiang, Z. Li, A. Han, J. Yu, S. Zhong, F. Meng, L. Zhang, Z. Liu, W. Liu, *Appl. Phys. Express.* **2022**, 15, 091001.
- [34] D. L. Staebler, C. R. Wronski, *J. Appl. Phys.* **1980**, 51, 3262.
- [35] Sentaurus Device User Guide, Synopsys, Inc., Mountain View, CA **2015**.